Article

Design of Metasurface-Based Photodetector with High-Quality Factor

Yu Geun Ki [ID], Hyeon Woo Jeon and Soo Jin Kim *[ID]

School of Electrical Engineering, Korea University, Seoul 02841, Republic of Korea; yu_geun_ki@korea.ac.kr (Y.G.K.); jeonhw9812@korea.ac.kr (H.W.J.)
* Correspondence: kimsjku@korea.ac.kr

Abstract: The ability of fine-tuning wavelengths in a high-Q resonance has been applied to various optical applications, particularly that of the development of nanoscaled, ultrathin photodetectors that realize next-generation optical sensors. However, designing a nanopatterned surface in a photodetector to induce intriguing optical effects inevitably deteriorates the electrical properties due to the increased roughness and defects, which cause the significant recombination of the photogenerated carriers. Moreover, light absorption in a semiconductor fundamentally decreases the Q factor of a resonance and ultimately limits the spectral sharpness. Thus, there is a trade-off between the applications of nano-optics for the fine control of wavelengths and the matured photodetector platform for electrical stability. In this work, we propose an alternative type of optical design for a photodetector by effectively decoupling the functionality of nano-optics for high-Q resonances and the electrical properties of semiconductors for the extraction of efficient photocarriers. By optimally balancing the loss of scattered radiation in a high-Q resonance and the loss of absorption in a semiconductor, we achieve a nano-optics-based photodetector with high-Q absorption and polarization sensing without a significant deterioration in the electrical properties. We believe that the suggested design rule can be effectively applied for the realization of emerging nanoscaled photodetectors for various applications of next-generation optical sensors.

Keywords: bound states in the continuum; metasurface; optoelectronics; photodetectors

1. Introduction

Harnessing nanoscaled resonances with a relatively high-quality (high-Q) factor have drawn attention from researchers over the last decades due to their potential applications to diverse fields in spectrometry, such as bio-optics, optical communications, and hyperspectral imaging [1–4]. High-Q resonance demonstrates the benefits of fine-tuning wavelengths to control, and it detects various types of optical information and can be used to mimic idealized optical filters. Such advancements in the nanoscaled high-Q platform are particularly important for the development of next-generation optical sensors as the era of IoT technology emerges. For example, high-Q metasurfaces operating at visible or near-infrared wavelengths can be integrated with compact form factors, such as augmented reality glassware or solid-state optical lidar, to manipulate light in an extraordinary way at the nanoscale level [5,6]. To accomplish the nanoscaled resonance with a high-Q factor, significant research efforts have been undertaken by exploring various nanostructures including surface relief gratings, photonic crystals, and metasurface-based bound states in the continuum (BIC) [7–13].

To progress the scientific efforts that have been undertaken to develop nanoscaled resonance at the device level, particularly that of developing a photodetector that targets the applications of optical sensors, various types of nanophotonic-based light detection mechanisms have been proposed and investigated. For example, by designing a surface patterned as a grating or nanopost array, researchers have demonstrated the ultrathin

types of photodetectors that absorb the targeted wavelength of light with relatively high-Q spectra [14–26]. Despite the progress that has been made, the Q factors of such proposed photodetectors are typically constrained by absorption in constituent, nanostructured semiconductors. Because the Q factor of a resonance is fundamentally limited by the dominant loss in the absorption or the scattered radiation from a resonator, inevitable absorption loss occurs in a resonant photodetector, which decreases and constrains the sensitivity of the spectral linewidth in spite of the strong confinement and negligible, scattered loss of light in a designed resonator [14–18]. Moreover, the patterning of a photodetector's surface typically induces significant photocarrier recombination and deteriorates the total performance of the photodetector by hindering internal quantum efficiency [19–24]. Thus, there has always been a trade-off between the employment of an emerging type of nanophotonic technology and the matured platform of conventional photodetectors in their optical and electrical efficiency.

In this work, we propose an alternative type of metasurface-based photodetectors that has both the optical advantage of nanoresonators and the electrical advantage of conventional photodetectors. Such an achievement is realized by effectively decoupling the high-Q resonance in nanostructured materials and the absorption in a conventional semiconductor layer. First, we design the Si_3N_4-based metasurface with high-Q, quasi-bound states in continuum (Q-BIC) to effectively capture and confine the incident light and thus enhance the Q factor, which is placed on top of a typical silicon photodetector. By effectively balancing the strength of the Q-BIC resonance in the Si_3N_4 layer with guided-mode resonance (GMR) in the silicon film, we can create a photodetector with enhanced spectral sensitivity without a significant decrease in quantum efficiency that typically occurs because of the recombination in nanostructured surfaces.

2. Design and Working Principles

The proposed device is schematically illustrated in Figure 1a. It consists of a silicon thin film, which is highlighted in red on a SiO_2 substrate in the figure. Moreover, the array of silicon nitride (Si_3N_4)-based nanoposts with an elliptical cross-sectional geometry is patterned on the silicon thin film. Additionally, metal electrodes are deposited at each end of the silicon film for extracting the current.
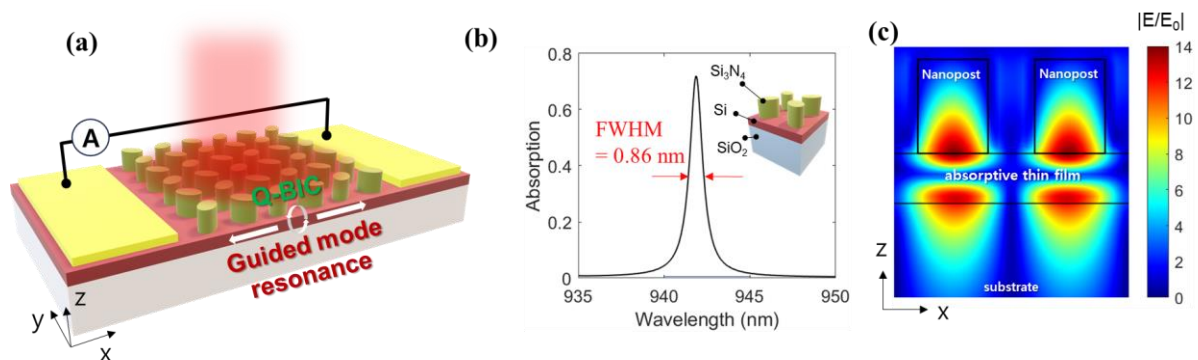
Figure 1. Proposed high-Q NIR photodetector. (**a**) Schematics of the high-Q NIR photodetector system consisting of an array of elliptical nanoposts (green) between the metal electrode (yellow) on the silicon guided layer (red). The closed circuit is formed by wire bonding at each electrode, and the photocurrent is measured by current meter as depicted by symbol A. (**b**) Simulated values of the absorption spectra of the proposed photodetector. (**c**) Electric field distribution unit cell elliptical nanoposts at the wavelength of 942 nm under the x-directed, linearly polarized light.

First, the elliptical nanopost array using silicon nitride (green) is designed on the silicon thin film to launch a Q-BIC through symmetry breaking. Next, the guided-mode resonance (GMR) upon the silicon thin film is excited through coupling with the Q-BIC along the Si_3N_4 pattern. The low radiative loss (high-Q factor) of the GMR and Q-BIC can be matched with the low absorption loss of the silicon at the near-infrared spectral

region, and thus high-Q absorption with a FWHM of 0.86 nm and a Q factor of 1148 at the silicon layer is achieved, as depicted in Figure 1b. More information regarding the coupling between the two resonances can be found in Figure 1c. It shows a strong electric field at the nanopost array by the excitation of Q-BIC under the x-directed linearly polarized light. In addition, an intense field is generated within the silicon film through the GMR in conjunction with the fields at the nanopost array. Owing to this strong field at the absorptive silicon layer, enhanced absorption can be achieved at the resonant frequency of interest. The detailed sizes and properties of the materials in the designed nanostructures are described in Figure 2. To evaluate the optical properties, simulated analysis using the finite-difference time-domain (FDTD) method is performed. The silicon film, which has a height of 160 nm (refractive index from the handbook of the optical constants of solids by Edward D. Palik, as shown in Supplementary Note S1 in Supplementary Materials file), is deposited on the glass substrate (refractive index of 1.45). Arrays of Si_3N_4 elliptical nanoposts (refractive index of 2.1) with a height of 300 nm are arranged on the silicon. Due to its moderate refractive index for Q-BIC coupling, the lossless property in the NIR region is compared with the significant losses in metal or silicon, and for acceptance in contemporary CMOS processes, Si_3N_4 is an effective option for high-Q resonance in optical applications. The period of arrays is designed to be 850 nm for both the x- and y-directions (Px, Py). The elliptical geometry is designed with the sizes of the long and short axes being 364 nm and 276 nm, respectively. The orientation angles of the long axis are a combination of 45° and 135°. All the parameters are targeted toward the NIR region for high-Q absorption in the silicon film. Moreover, the minimum gap between the nanoposts is set to be larger than 100 nm for a reliable practical fabrication process, as described in Supplementary Note S2. In the unit cell, the periodic boundary condition is applied along the x- and y-directions, and the perfectly matched layer absorbing boundary conditions are applied along the z-direction. Transmission and reflection are calculated by monitoring the power in a far-field regime. Absorption is calculated using the transmission and reflection values.
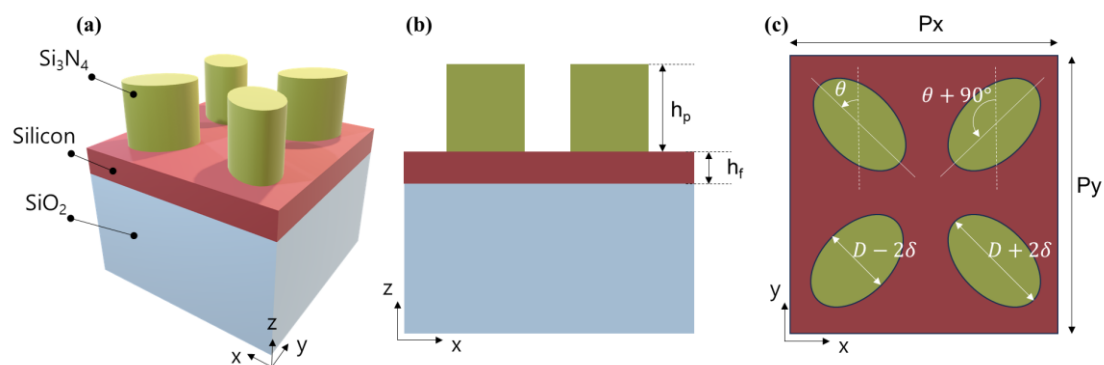

Figure 2. Geometric parameters of the unit cell structure. (**a**) Schematic view of the unit cell composed of the glass substrate, silicon thin film, and nanoposts with Si_3N_4. (**b**) Side view of the unit cell with the 300 nm height of the nanopost (h_p) and the 160 nm height of the silicon film (h_f) (**c**) Top view of the unit cell with the Px and Py of 850 nm, D of 320 nm, δ of 22 nm, and θ of 45°.

2.1. Quasi-Bound States in the Continuum (Q-BIC) at the Nanopost Array

To better understand the operating principles of the proposed photodetector, Figure 3 shows the analysis of the Q-BIC that is excited by the Si_3N_4 nanopost array. Firstly, to analyze the Q-BIC without coupling with the GMR, Figure 3a–d show the analysis of the metasurface without the addition of the silicon film, i.e., with silicon thickness (h_f) being 0 nm. A true BIC or symmetry-protected BIC is a state that can only exist for ideal cases. It has an infinite value for the Q factor and a zero full-width at the half-maximum (FWHM). Any variation that breaks the in-plane inversion symmetry turns the true BIC into the Q-BIC with a finite but still high-Q factor. The difference (δ) in the length between the ellipses' major and minor axes is an asymmetry parameter in our design. The Q-BIC can be excited

by placing elliptical nanoposts ($\delta > 0$) tilted with θ being 45° and 135° diagonally. Two opposing y-directed resonant dipoles (arrows in Figure 3c) are induced, and the support dark mode resonance (Q-BIC) is induced when the long axis of the ellipsoids is oriented as a combination of 45° and 135°. This is visualized through the magnetic fields that are oriented out of the plane by momentum transfer under x-polarized light (Figure 3c). Due to the geometric properties of the unit cells that satisfy C_4 symmetry, such a Q-BIC can be also observed under y-polarized light with different field distributions with two oppositely x-directed electric dipoles. The sharp Lorentzian shape in the reflection spectra of Figure 3d is due to the high-Q nature of the Q-BIC. Figure 3b,c show the strong electric and magnetic fields at this resonant frequency.
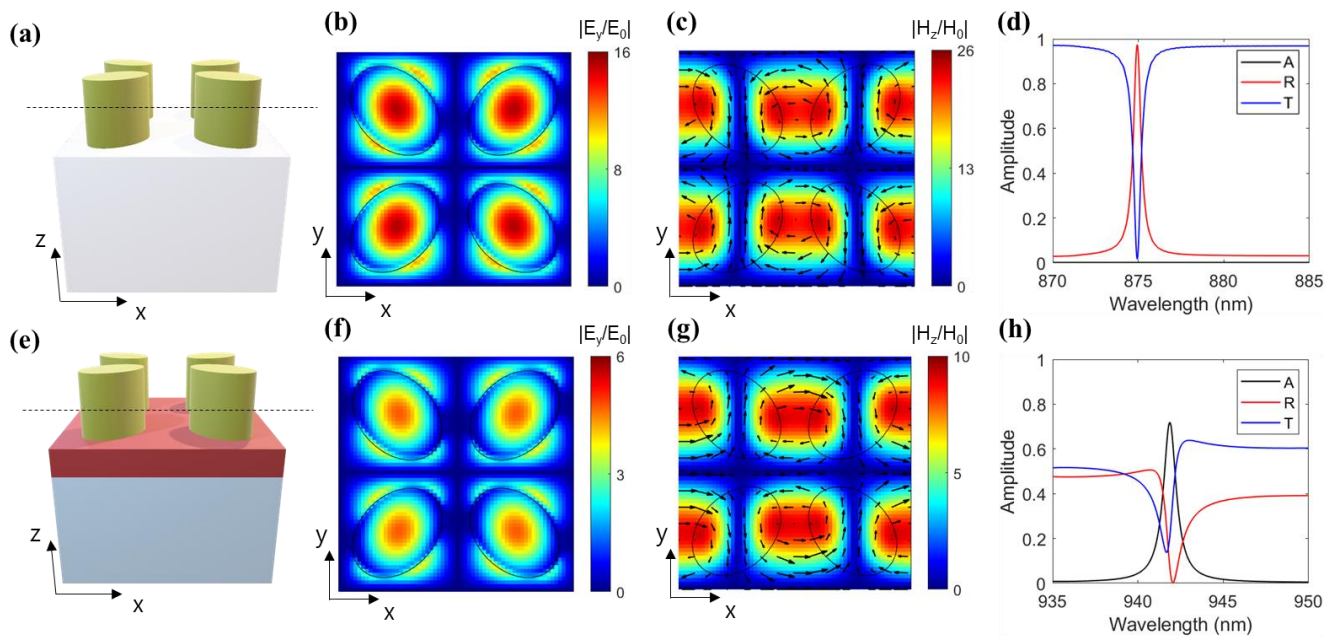
Figure 3. Analysis of a Q-BIC at the nanopost array. (**a**) Schematics of the metasurface with a silicon thickness (h_f) of 0 nm. (**b**,**c**) Simulated electric and magnetic field distributions. Arrows in (**c**) indicate the directions of the electric field. The black solid lines indicate the boundaries of elliptical nanoposts. (**d**) Absorption, transmission, and reflection spectra of the metasurface. (**e**) Schematics of the metasurfaces with a silicon thickness (h_f) of 160 nm. (**f**,**g**) Simulated electric and magnetic field distributions. Arrows in (**g**) indicate the directions of the electric field. The black solid lines indicate the boundaries of elliptical nanoposts. (**h**) Absorption, transmission, and reflection spectra of the metasurface.

Next, the behavior of the Q-BIC with the presence of the silicon film that has a 160 nm height supporting the GMR is depicted in Figure 3e–h. The field distributions in Figure 3f,g exhibit that the Q-BICs akin to those in Figure 3b,c are excited. However, additional coupling with the GMR with absorptive silicon leads to a different spectral shape in the absorption, reflection, and transmission spectra, as displayed in Figure 3h. Fano-shaped spectra can be seen in the transmission and reflection, thereby indicating the mutual coupling between the two distinct modes. The high field intensity in the absorptive layer due to the coupling produces a high-Q absorption spectrum (Figure 1c).

2.2. The Control of the Asymmetrical Parameter to Match the Radiation Loss with the Absorption Loss of a Silicon Thin Film

It is important to understand the relationship between a Q factor and the losses that occur in a resonant system. Losses in a resonant system are accounted for two factors, i.e., an absorption loss and a radiation loss. The first factor of absorption loss is caused by the absorption of light in a material, which is intrinsically induced as far as the specific

condition is satisfied whereby the bandgap energy of a material is smaller than the photon energy of light. Thus, inevitable loss is included in a resonant photodetector system that is operated through being based on solid-state semiconductors. The second factor of radiation loss is generated by the scattering or re-radiation of light during a resonance occurring in a resonant system. While the significant energy portion of incident light is typically coupled with the resonant system, the partial energy portion of the light is scattered by the reflection from the nanostructured surface of a designed material. In addition to being scattered by the reflection, the coupled light, which is confined to the resonant system, is re-radiated toward the free space or back toward the superstrate of the side of light incidence after circulating inside the resonator. Such re-radiation is also inevitable as long as the resonant system is not completely closed from the free space. In other words, an open resonant system couples the incident light from the free space and re-radiates it back toward the free space after the resonance that is based on the fundamental reciprocity mechanism in optics. In particular, nanostructured resonant systems or nanophotonic systems show relatively inferior abilities in confining light compared with the micro-resonant system, such as whispering gallery modes in the microsphere, and thus the scattering or re-radiation of light from the nanophotonic system is more significant than the traditional micro-optic examples. Thus, it is an attractive field of research, and significant research has been conducted to enhance light confinement in a nanostructured resonant system. Based on the aforementioned mechanism, the total Q factor of a resonant system is determined by the Q factor constrained by the absorption loss and the Q factor constrained by the radiation loss, i.e., scattering and re-radiation during a resonance. Notably, the total Q factor (Q_{tot}) is dominantly constrained by the minimum value in the Q factor by absorption (Q_{abs}) and the Q factor by radiation (Q_{rad}) and is thus expressed by the following equation:

$$1/Q_{tot} = 1/Q_{abs} + 1/Q_{rad} \tag{1}$$

The absorption Q factor (Q_{abs}) increases as the imaginary part of the refractive index of a material decreases since a decrease in the degree of absorption enhances light confinement inside a resonant system. The radiation Q factor (Q_{rad}) increases as the designed resonant system effectively confines the coupled light inside a resonator and radiates less back toward the free space, which increases the circling cycle of light in a resonator. Since the Q_{abs} is determined through the properties of the materials, i.e., the imaginary part of the refractive index, Q_{rad} is typically engineered by structuring the nanostructures to enhance the quality factor of an entire resonant system, i.e., to enhance the sharpness of the resonant spectra.

As the next stage, to maximize the absorption rate, the effect of the geometric variation in the ellipses on the absorptivity is analyzed. Such a geometric perturbation is conducted by breaking the geometric symmetry of the nanoposts, which are denoted as δ, to create a minor axis and a major axis, as indicated in Figure 2c. Since this perturbation launches the Q-BIC, the degree of perturbation leads to the different coupling strengths against light, and such strength of coupling is typically estimated by the degree of Q factors, i.e., the radiation Q factor of the Q-BICs can be modified by adjusting geometrical perturbation δ. For example, as the perturbation increases, light is more strongly coupled with and more strongly re-radiates from the resonator, and the Q factor decreases as the leakage of light by the radiation increases.

Based on the aforementioned principles, the absorption of the designed photodetector is analyzed by changing the degree of asymmetry, as illustrated in Figure 4. To represent the difference in axes compared with the overall size of the ellipse, we set the relative asymmetry parameter α according to the following equation:

$$\alpha = 2\,\delta/D \tag{2}$$
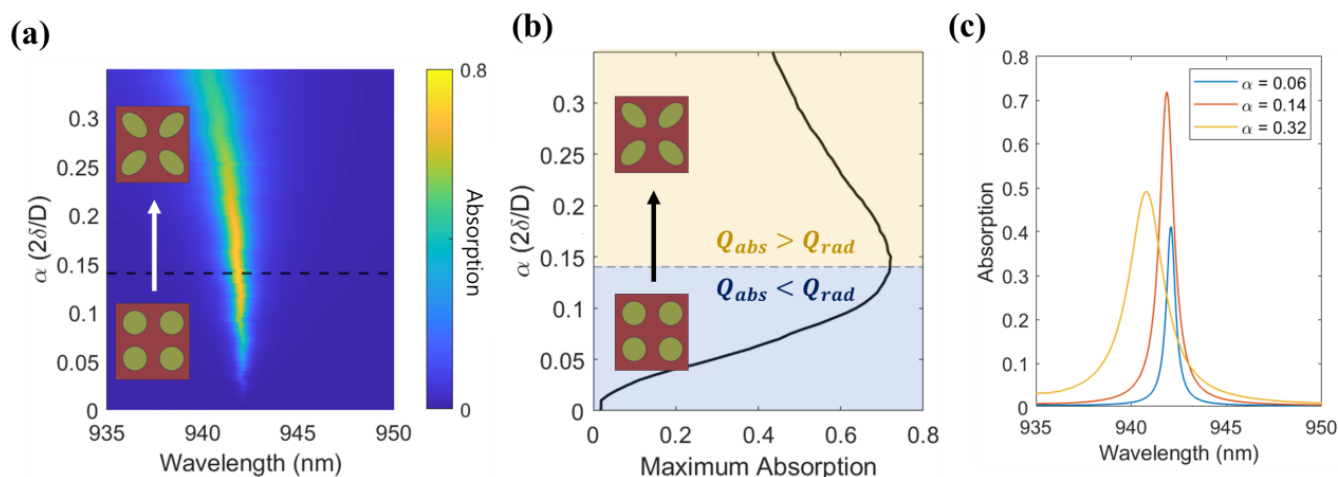
Figure 4. Control of the relative asymmetry parameter to match the radiation loss with the absorption loss. (**a**,**b**) Absorption spectra for the continuously changing asymmetry parameter α ($2\delta/D$) of the high-Q photodetector under x-polarized incident light (**a**) and the maximum absorption at the spectral peaks of each α value (**b**). The vertical arrows in the panels highlight the geometric design evolved from circles to ellipses. (**c**) Absorption spectra of the high-Q photodetector with $\alpha = 0.06$ (blue), $\alpha = 0.14$ (orange), and 0.32 (yellow).

From Figure 4a, the absorption peak near the wavelength of 940 nm is observed in the overall changes in α. To maintain the resonant frequency, we control the relative asymmetry parameters of δ ranging from 0 to 50 nm. Specifically, the absorptivity gradually increases to the maximum value as the α changes from 0 to 0.14 and then decreases as the α continues to increase over 0.14. The spectral peaks of the absorption are evaluated and visualized in Figure 4b, which shows that the absorption monotonically increases as α increases up to 0.14 and reaches the maximum value of 0.71. Figure 4c shows the three representative spectra at the α of 0.06, 0.14, and 0.31, which show the maximized absorption at the α of 0.14. It is important to note that the FWHM of the spectra monotonically increases and the spectra broaden as the α increases. This means that the radiation Q factor (Q_{rad}) continues to decrease as the α increases. At a design range of α below 0.14, although the Q_{rad} decreases with an increased α, the Q_{rad} is relatively higher than the absorption Q factor (Q_{abs}), or, equivalently, the radiation loss is lower than the absorption loss. In this condition, the Q_{abs} constrains the enhancement of the total Q factor (Q_{tot}) and is the limiting factor. On the other hand, as the α increases above 0.14, the Q_{rad} is lower than the Q_{abs}, and the Q_{rad} thus becomes the limiting factor against the enhancement of the Q_{tot}. At the α of 0.14, the Q_{rad} closely matches the Q_{abs}, which optimizes the coupling of light and thus maximizes the absorption.

3. Results

3.1. High-Q Photodetector with Polarization Sensing

To find the effect of the lattice size and different θ values of the metasurface geometry on the property of high-Q resonances, Figure 5 illustrates the absorption contrast under each orthogonal, linearly polarized light. As shown in Figure 5a, the metasurface designed at the rectangular lattice (Px = 875 nm and Py = 825 nm) exhibits the shifting and switching of the absorption peaks depending on the state of linear polarization. For each linear polarization, the magnetic fields at each resonant frequency of 941 nm and 945 nm are shown in Figure 5b,c, respectively. The distributions of the magnetic fields under x- and y-polarizations in Figure 5b,c are akin to the result of the square lattice depicted in Figure 3g. This confirms that the near-identical mode of the BIC resonance can be supported under both forms of linearly polarized light. In Figure 5b under the x-polarized incident light, the strong magnetic field-oriented out-of-plane direction induces electric dipoles in the

y-direction. In Figure 5c, under the y-polarized incident light, the strong magnetic field is displayed, and electric dipoles are induced in the x-direction by the magnetic field as opposed to the y-directed electric dipoles depicted in Figure 5b. It is also worth noting that a slight blue shift (940 nm) in the spectral peak of absorption compared with the original design in Figure 4 occurs because of a modest decrease in Py. On the contrary, due to the increased Px, the redshift in the absorption peak at (944 nm) is observed. Similarly, the resonance frequency under each linearly polarized light varies and can be controlled by designing the difference between Px and Py.
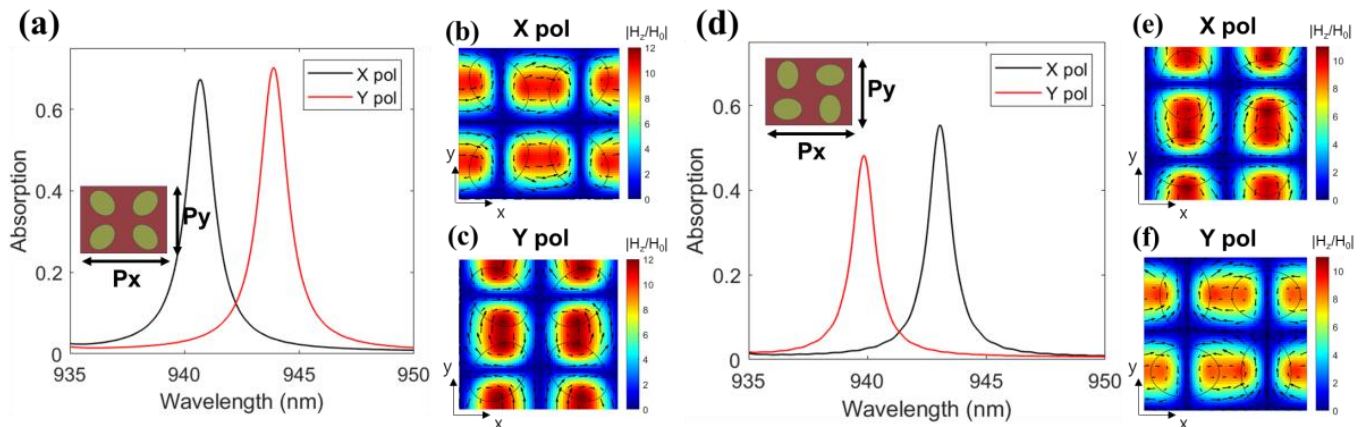
Figure 5. High-Q NIR photodetector for linear polarization sensing. (**a**) Absorption spectra of the proposed photodetector with rectangular lattice under both linear polarizations. (**b**,**c**) Simulated field distribution under x- and y-polarized incident light at each resonant frequency. Arrows indicate the directions of the electric field. The black solid lines indicate the boundaries of elliptical nanoposts. (**d**) Absorption spectra of another type of symmetry breaking ($\theta = 0°$) under each orthogonal, linear polarization. (**e**,**f**) Simulated field distribution for x- and y-polarized light at each resonant frequency. Arrows indicate the directions of the electric field. The black solid lines indicate the boundaries of elliptical nanoposts.

Furthermore, the analysis of the high-Q photodetector with the ellipsis orientations of $\theta = 0°$ is shown in Figure 5d,e. Notably, when $\theta = 0$, the x-polarized incident light induces x-directed electric dipoles, which are in opposite directions to the dipole orientation of the adjacent cells. The overall field distribution under the y-polarized light in Figure 5c and the overall field distribution under the x-polarized light in Figure 5d are close to being identical to the direction that is parallel to each polarized direction. There is a minor difference in the modified orientations (θ) of the elliptical nanoposts in Figure 5d compared with the case in Figure 5a in the splitting of the resonant peaks in the opposite way which was observed for them. As a result, when $\theta = 0$, the higher Px causes the resonance frequency under the x-polarized light to redshift, and significant absorption happens at 944 nm under the x-polarized light. Similarly, under the y-polarized light (Figure 5e), the field resembles that which was observed under the x-polarized light (Figure 5b), and the decrease in Py causes a blue shift in the absorption spectra.

Based on the presented design and analysis, the targeted polarization and wavelength can be adjusted through the lattice parameters (Px, Py) and appropriate symmetry breaking (θ) without any significant modifications in the analyzed high-Q resonant mode, which confirms the effective utilization of the designed metasurface as a photodetector used for polarization sensing.

3.2. High-Q Photodetector for Refractive Index Sensing

Refractive index variations can be detected by observing the shift in the optical resonant frequency of the sensors when a certain target material is present on its surface. A high-Q factor of the optical sensor is necessary in order to identify tiny variations in

refractive index. Most of the reported metasurface-based refractive index sensors make use of either transmission or reflection in their sensing of the index since the Q factor of the absorption is relatively low and is difficult to use for subtle changes in the optical environment. Figure 6 illustrates how the designed photodetector has the ability to overcome these limits. Figure 6 displays the absorption spectra of the metasurface at different superstrate refractive indices ranging from 1 to 1.3. As the refractive index of the superstrate increases larger than 1, the absorption peak is redshifted. Such a redshift is caused by the increase in the effective index of the metasurface layer which is the mixture of resonant Si_3N_4 nanoposts and superstrate index. It is important to note that the high-Q absorption peak can function as a steady refractive index sensor because it only varies in resonant frequency and not in FWHM or absorption rate. The slight shift can be distinguished owing to its high-Q factor and small spectral width. Figure 6b illustrates the significant shift in resonant frequency (67 nm per refractive index resolution (RIU)). These results imply that the resonant frequency of the high-Q photodetector can be easily tuned by the subtle changes of the background refractive index, which shows the potential applications to biosensing in the NIR spectral range.
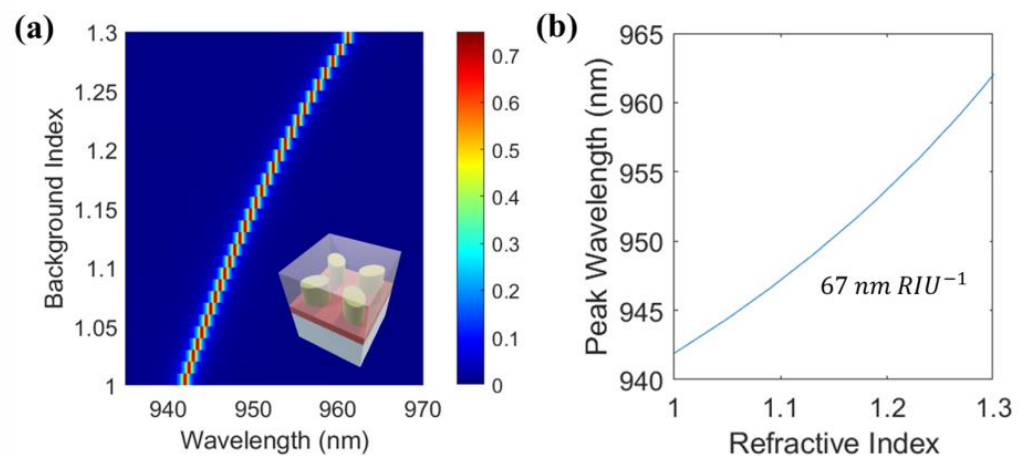
Figure 6. High-Q NIR photodetector for refractive index sensing. (**a**) Simulated absorption spectra of a high-Q photodetector for various background refractive indices. (**b**) Resonance peak position as a function of the background refractive index. It shows the sensitivity of 67 nm to be RIU^{-1}.

4. Discussion

Table 1 summarizes and compares the optical performance with the previously remarkable design of photodetectors based on metasurfaces. The FWHM of the devices was fundamentally limited by the dominant loss among the absorption of the high refractive index materials like germanium. Additionally, patterning a photodetector surface usually results in a large amount of photoelectron recombination, which potentially lowers the overall performance of photodetectors by hindering internal quantum efficiency. Alternatively, designs using cavities or two-dimensional materials have been reported, which could be a promising solution for future photodetectors; however, there was limited compatibility with the sophisticated platform of conventional photodetectors.

Our alternative type of metasurface-based photodetector shows enhanced spectral sensitivity with a FWHM of 0.82 nm without a cavity structure and 2D materials such as graphene. Moreover, this induces absorption in a silicon thin film and minimizes the defects that may arise during the patterning processes, which ultimately could achieve a high absorption rate of over 0.7.

Table 1. Comparison with previously reported metasurface-based photodetectors. Our work demonstrates outstanding results with a relatively simple configuration that can be created using a CMOS-compatible process. It exhibits a moderate absorption rate and an extremely narrow resonance peak in the NIR region. Additionally, it can extract a photocurrent through the silicon film, thereby minimizing the recombination of photocarriers.

Ref.	Material	Configuration	Absorption (Simulated)	Operating Wavelength	FWHM	Q Factor	Path of Photo-electrons
[14]	Ge	Ge film and circular nanoposts	0.6	1570 nm	98 nm	16	Ge film
[15]	Ge	Ge film and circular nanoposts	1	1000–1600 nm	Over 600 nm	NA	Ge film
[19]	Si, Ag	Si nanowire in Ag substrate	0.8	595 nm, 625 nm	Over 36 nm	17	Si nanowire
[25]	Ge, Si	Cavity with Silicon nanoposts and Ge thin film	0.92	1242 nm	4.4 nm	282	Ge film
[27]	Graphene, Au	Cavity with silicon nanowire and metallic mirror; graphene is on the nanowire	1	1350 nm	6 nm	225	Graphene
[28]	Si, Graphene	Graphene on Si circular nanoposts with a nanohole	0.5	1400 nm	4 nm	350	Graphene
[29]	Graphene, Au	Au split-ring structure on graphene	1	1550 nm	343 nm	4	Graphene
Our work	Si, Si_3N_4	Si_3N_4 elliptical nanoposts on Si film	0.7	942 nm	0.82 nm	1148	Si film

5. Conclusions

In summary, we propose a high-Q metasurface photodetector that can be achieved by effectively decoupling the absorption in a conventional semiconductor layer with the high-Q resonance in nanostructured materials. We designed a highly narrow resonance with a moderate absorption rate, which was excited by the Q-BIC, by achieving the proper degree of symmetry breaking. Furthermore, the proposed photodetector has improved the spectral sensitivity without appreciably lowering its quantum efficiency by effectively preventing the significant carrier's recombination, which occurred in a resonant nanostructured surface.

With the proposed photodetector, we demonstrate efficient polarimetric detection and refractive index sensing for the potential applications of spectropolarimetry and biosensing. Moreover, our design concepts, which make use of a lossless nanoposts array and an absorptive thin film, are expected to be applied to a variety of wavelength ranges, including visible and MIR ones, in addition to the proposed NIR region. The presented study has the potential to reveal new possibilities for numerous optical applications, including next-generation optical sensors.

Supplementary Materials: The following supporting information can be downloaded at: https://www.mdpi.com/article/10.3390/electronics13040753/s1, Supplementary Note S1. The refractive index of silicon. Figure S1. Fitted real(n) and imaginary(k) parts of the refractive index of crystalline silicon. The refractive index for each wavelength was fitted based on Palik's handbook [30]. Supplementary Note S2. Fabrication process of the high-Q photodetector. Figure S2. Schematics of the fabrication process of the proposed metasurface. Supplementary Note S3. Impact of nonuniformity of nanoposts. Figure S3. Analysis of performance degradation due to nonuniformity of geometric parameters because of imperfect fabrication process. (a–c) Schematic of the simulated group cell for the process. Three targeted geometric parameters of each nanoposts are set differently. (d–f) Distributions of the D(d), δ(e), and θ(f) for each unit cell of the simulated group cell. (g–i) Simulated absorption, reflection, and transmission for four group cells with different geometric distributions. Supplementary Note S4. Impact of the overall size of the ellipses. Figure S4. Impact of the overall size of the nanoposts. (a) Colormap of absorption spectra obtained by varying diameter of nanoposts while keeping relative asymmetry parameter α described in Equation (2). (b). Absorption spectra for each diameter with a fixed α. (c, d). Simulated electric and magnetic field distributions for D = 360 nm and D = 290 nm. Arrows indicate the directions of the electric field.

Data Availability Statement: All data are available from the authors on reasonable request.

Conflicts of Interest: The authors declare no conflicts of interest.

References

1. Yang, Y.; Kravchenko, I.I.; Briggs, D.P.; Valentine, J. All-dielectric metasurface analogue of electromagnetically induced transparency. *Nat. Commun.* **2014**, *5*, 5753. [CrossRef] [PubMed]
2. Tittl, A.; Leitis, A.; Liu, M.; Yesilkoy, F.; Choi, D.-Y.; Neshev, D.N.; Kivshar, Y.S.; Altug, H. Imaging-based molecular barcoding with pixelated dielectric metasurfaces. *Science* **2018**, *360*, 1105–1109. [CrossRef] [PubMed]
3. Huang, L.; Jin, R.; Zhou, C.; Li, G.; Xu, L.; Overvig, A.; Deng, F.; Chen, X.; Lu, W.; Alù, A. Ultrahigh-Q guided mode resonances in an All-dielectric metasurface. *Nat. Commun.* **2023**, *14*, 3433. [CrossRef] [PubMed]
4. Hu, H.; Weber, T.; Bienek, O.; Wester, A.; Huttenhofer, L.; Sharp, I.D.; Maier, S.A.; Tittl, A.; Cortés, E. Catalytic Metasurfaces Empowered by Bound States in the Continuum. *ACS Nano* **2022**, *16*, 13057–13068. [CrossRef]
5. Song, J.-H.; van de Groep, J.; Kim, S.J.; Brongersma, M.L. Non-local metasurfaces for spectrally decoupled wavefront manipulation and eye tracking. *Nat. Nanotechnol.* **2021**, *16*, 1224–1230. [CrossRef] [PubMed]
6. Malek, S.C.; Overvig, A.C.; Alù, A.; Yu, N. Multifunctional resonant wavefront-shaping meta-optics based on multilayer and multi-perturbation nonlocal metasurfaces. *Light Sci. Appl.* **2022**, *11*, 246. [CrossRef]
7. Ji, A.; Song, J.-H.; Li, Q.; Xu, F.; Tsai, C.-T.; Tiberio, R.C.; Cui, B.; Lalanne, P.; Kik, P.G.; Miller, D.A.B.; et al. Quantitative phase contrast imaging with a nonlocal angle-selective metasurface. *Nat. Commun.* **2022**, *13*, 7848. [CrossRef]
8. Born, B.; Lee, S.-H.; Song, J.-H.; Lee, J.Y.; Ko, W.; Brongersma, M.L. Off-axis metasurfaces for folded flat optics. *Nat. Commun.* **2023**, *14*, 5602. [CrossRef]
9. Wang, K.; Gu, T.; Bykov, D.A.; Zhang, X.; Qian, L. Tunable nanolaser based on quasi-BIC in a slanted resonant waveguide grating. *Opt. Lett.* **2023**, *48*, 4121–4124. [CrossRef]
10. Guo, C.; Xiao, M.; Orenstein, M.; Fan, S. Structured 3D linear space–time light bullets by nonlocal nanophotonics. *Light Sci. Appl.* **2021**, *10*, 160. [CrossRef]
11. Piper, J.R.; Fan, S. Total absorption in a graphene monolayer in the optical regime by critical coupling with a photonic crystal guided resonance. *ACS Photonics* **2014**, *1*, 347–353. [CrossRef]
12. Tian, J.; Li, Q.; Belov, P.A.; Sinha, R.K.; Qian, W.; Qiu, M. High-Q all-dielectric metasurface: Super and suppressed optical absorption. *ACS Photonics* **2020**, *7*, 1436–1443. [CrossRef]
13. Overvig, A.C.; Malek, S.C.; Carter, M.J.; Shrestha, S.; Yu, N. Selection rules for quasibound states in the continuum. *Phys. Rev. B* **2020**, *102*, 035434. [CrossRef]
14. Zhou, Z.-X.; Ye, M.-J.; Yu, M.-W.; Yang, J.-H.; Su, K.-L.; Yang, C.-C.; Lin, C.-Y.; Babicheva, V.E.; Timofeev, I.V.; Chen, K.-P. Germanium metasurfaces with lattice kerker effect in near-infrared photodetectors. *ACS Nano* **2022**, *16*, 5994–6001. [CrossRef]
15. Yezekyan, T.; Zenin, V.A.; Thomaschewski, M.; Malureanu, R.; Bozhevolnyi, S.I. Germanium metasurface assisted broadband detectors. *Nanophotonics* **2023**, *12*, 2171–2177. [CrossRef]
16. Đorđević, N.; Schwanninger, R.; Yarema, M.; Koepfli, S.; Yarema, O.; Salamin, Y.; Lassaline, N.; Cheng, B.; Yazdani, N.; Dorodnyy, A.; et al. Metasurface Colloidal Quantum Dot Photodetectors. *ACS Photonics* **2022**, *9*, 482–492. [CrossRef]
17. Sharma, N.; Bar-David, J.; Mazurski, N.; Levy, U. Metasurfaces for Enhancing Light Absorption in Thermoelectric Photodetectors. *ACS Photonics* **2020**, *7*, 2468–2473. [CrossRef]
18. He, J.; Li, C.-Y.; Qi, D.-X.; Cai, Q.; Liu, Y.; Fan, R.-H.; Su, J.; Huo, P.; Xu, T.; Peng, R.; et al. Improving Photoelectric Conversion with Broadband Perovskite Metasurface. *Nano Lett.* **2022**, *22*, 6655–6663. [CrossRef] [PubMed]
19. Kim, S.J.; Kang, J.-H.; Mutlu, M.; Park, J.; Park, W.; Goodson, K.E.; Sinclair, R.; Fan, S.; Kik, P.G.; Brongersma, M.L. Anti-Hermitian photodetector facilitating efficient subwavelength photon sorting. *Nat. Commun.* **2018**, *9*, 316. [CrossRef]
20. Kim, S.J.; Lee, C.; Jeon, S.; Park, J.; Kim, S.J. Subwavelength sorting of full-color based on anti-Hermitian metasurfaces. *Nanophotonics* **2020**, *10*, 967–974. [CrossRef]
21. Hong, J.; van de Groep, J.; Lee, N.; Kim, S.J.; Lalanne, P.; Kik, P.G.; Brongersma, M.L. Nonlocal metasurface for circularly polarized light detection. *Optica* **2023**, *10*, 134–141. [CrossRef]
22. Chen, Z.; Weng, Y.; Liu, J.; Guo, N.; Yu, Y.; Xiao, L. Dual-band perfect absorber for a mid-infrared photodetector based on a dielectric metal metasurface. *Photon. Res.* **2021**, *9*, 27–33. [CrossRef]

23. Hainey, M.F.; Mano, T.; Kasaya, T.; Ochiai, T.; Osato, H.; Watanabe, K.; Sugimoto, Y.; Kawazu, T.; Arai, Y.; Shigetou, A.; et al. Near-field resonant photon sorting applied: Dual-band metasurface quantum well infrared photodetectors for gas sensing. *Nanophotonics* **2020**, *9*, 4775–4784. [CrossRef]
24. Mitrofanov, O.; Hale, L.L.; Vabishchevich, P.P.; Luk, T.S.; Addamane, S.J.; Reno, J.L.; Brener, I. Perfectly absorbing dielectric metasurfaces for photodetection. *APL Photonics* **2020**, *5*, 101304. [CrossRef]
25. Yu, J.; Ma, B.; Qin, R.; Ghosh, P.; Qiu, M.; Li, Q. High-Q absorption in all-dielectric photonics assisted by metamirrors. *ACS Photonics* **2022**, *9*, 3391–3397. [CrossRef]
26. Li, J.; Li, J.; Zhou, S.; Yi, F. Metasurface Photodetectors. *Micromachines* **2021**, *12*, 1584. [CrossRef]
27. Jin, R.; Huang, L.; Zhou, C.; Guo, J.; Fu, Z.; Chen, J.; Wang, J.; Li, X.; Yu, F.; Chen, J.; et al. Toroidal Dipole BIC-Driven Highly Robust Perfect Absorption with a Graphene-Loaded Metasurface. *Nano Lett.* **2023**, *23*, 9105–9113. [CrossRef] [PubMed]
28. Wang, X.; Duan, J.; Chen, W.; Zhou, C.; Liu, T.; Xiao, S. Controlling light absorption of graphene at critical coupling through magnetic dipole quasi-bound states in the continuum resonance. *Phys. Rev. B* **2020**, *102*, 155432. [CrossRef]
29. Attariabad, A.; Pourziad, A.; Bemani, M. A tunable and compact footprint plasmonic metasurface integrated graphene photodetector using modified omega-shaped nanoantennas. *Opt. Laser Technol.* **2022**, *147*, 107660. [CrossRef]
30. Palik, E.D. *Handbook of Optical Constants of Solids*; Academic Press: Cambridge, MA, USA, 1998; Volume 3.